# Loss of *cep57* function induces G1 arrest and microcephaly

Sharada Iyer[1,2], Advait Gokhale[1], Pooja Shree Murugesan[1], Megha Kumar[1,2*]

[1]CSIR-Centre for Cellular and Molecular Biology (CSIR-CCMB), Habsiguda, Uppal road, Hyderabad-50007, India

[2]Academy of Scientific and Innovative Research (AcSIR), Ghaziabad-201002, India

[*]Correspondence:

Megha Kumar, Ph.D.

Senior Scientist

W107 CSIR-CCMB, Habsiguda, Uppal Road, Hyderabad 500007

Telangana, India

Email: meghakumar@ccmb.res.in

ORCID: 0000-0002-3842-9975

**Abstract**

Centrosomal protein 57 (CEP57) is essential for centrosome organization, regulating nucleation and stabilization of microtubules, and mitotic spindle formation. Here, we uncover uncharacterized, distinct functions of *cep57* in modulating cell cycle progression, spindle pole integrity and directing cranial neural crest specification during early embryonic development. We demonstrate that *cep57* localizes to both the nucleus and centrosomes in zebrafish blastulae, and its depletion results in spindle pole focusing defects and G1 phase arrest. Additionally, the *cep57* deficient embryos exhibit increased apoptosis, disrupted cranial neural crest specifiers, and microcephaly-associated characteristics. The comparative proteome analysis reveals a previously uncharacterized role of Cep57 in regulating G1 arrest and DNA damage-related proteins, including Dapk1, Arid3B, Cpped1, Pp2a, and Annexin V, as well as key cell cycle modulators such as Smc4, 14-3-3, Ctf8, and CDK7. Hence, this study highlights the broader, multifaceted role of *cep57* in cell cycle progression and early neurodevelopment with fresh insights into its functional significance beyond centrosome regulation.

**Keywords:**

Centrosome, Cep57, cell cycle, microcephaly, apoptosis

## Introduction:

Centrosomal protein 57 (CEP57) plays key roles in centriole dynamics, mitotic spindle assembly, and organization. It is essential for pericentriolar matrix (PCM) organization, centriole duplication, and engagement. Lack of CEP57 results in PCM disorganization and precocious centriole disengagement, resulting in ectopic MTOCs and chromosome segregation errors.[1–7] CEP57 is also essential for the nucleation and stabilization of microtubules and spindle formation, and its depletion results in misaligned chromosomes, multipolar spindles, and PCM fragmentation.[4,8,9] Thus, CEP57 is essential for both spindle pole integrity and also acts as an MT stabilizing factor to aid in the formation of the bipolar spindle.[9,10] Further, it localizes to the kinetochores and interacts with microtubules to remove Mad1 from the kinetochores, and its depletion results in impaired SAC signaling and chromosome segregation defects. These studies show that CEP57 functions to maintain SAC activation and correct chromosome segregation.[7,9,11] CEP57 also localizes to the cytokinetic midbody and aids in central spindle microtubule organization.[12]

Mutations in the *CEP57* gene are associated with Mosaic Variegated Aneuploidy syndrome (MVA). MVA is an autosomal recessive disorder characterized by chromosome gain or loss in somatic cells, which results in mosaic aneuploidies. These patients show microcephaly, skull deformities, facial dysmorphism, and predisposition to tumors. [1,6,13–15] The *Cep57* knockout was embryonic lethal, and the heterozygous mice exhibited severe vertebrate ossification defects and died shortly after birth. The cells of knockout mice showed aneuploidy, impaired centrosomal maturation, premature centriole disjunction, and chromosome segregation anomalies.[4,16] However, the mechanisms of microcephaly mutations in h*CEP57* remain unknown. These centrosomal and chromosomal segregation defects may be the underlying basis of the reduced number of neural progenitor cells, resulting in microcephaly. To test this hypothesis, we investigated the role of *cep57* in embryonic mitoses and cranial neural crest progenitor cells, which give rise to the neural tissues, using a gene knockdown approach, extensive expression analyses, and mass spectrometry-based comparative proteomic analysis. Our results show that *cep57* localizes to the spindle poles at metaphase and nucleus in the zebrafish blastulae. During early embryogenesis, *cep57* is essential for brain, somite, and anteroposterior axis patterning. The morphants showed downregulation of neural crest specifier genes and mesodermal defects,

suggesting that *cep57* is essential to maintain the progenitor cell fate in the cranial neural crest. *Cep57* depletion also resulted in microcephaly-allied phenotypes such as reduced interpupillary distance and decreased expression of microcephaly-associated genes. Intriguingly, the morphants showed an increase in the G1 phase with a concomitant reduction in the G2/M phase, coupled with extensive apoptosis and increased genomic instability. We show that *cep57* is essential for cell cycle progression, neural crest specification, and survival. This *cep57*-mediated cell cycle regulation in neural progenitors provides fresh perspectives to the h*CEP57*-associated MVA and microcephaly.

**Results:**

**Cep57 localizes to the nucleus, spindle poles and is essential for early neurodevelopment**

We first examined the spatiotemporal expression pattern of *cep57* across the developmental stages of zebrafish embryos. *Cep57* was ubiquitously expressed at cleavage stages, indicating that it is maternally inherited till gastrulation (red asterisk, Fig. 1A, B). The expression was restricted to the eye and brain during somitogenesis until 24hpf (double red asterisk, Fig. 1A). Cep57 protein levels were also maintained across early developmental stages till 1dpf (Fig. S1A). In early blastomeres, Cep57 localized to the spindle poles at metaphase (red asterisks, Fig. 1C) and in the nucleus (Fig. 1D). To ascertain the developmental functions of *cep57*, we used a gene knockdown approach using antisense morpholinos (translation and splice blocker) against zebrafish *cep57*. Cep57 depletion was confirmed by immunoblotting with the morphant lysates (Fig. 1E). The *cep57* translation blocker morphants showed somitic defects (red asterisk, Fig. 1G), abnormalities in the brain architecture and organization, eye and otic vesicle defects (double red asterisks, Fig. 1G) along with a poorly developed anteroposterior axis (red arrow, Fig. 1G). We categorized the morphants as normal, like controls (P0), embryos with brain abnormalities (P1, 41.4%), embryos with brain abnormalities and anterior-posterior axis defects (P2, 38.41%), and the extremely severe phenotype with poorly developed brain and body axis (P3, 15.78%) (Fig. 1G, S1B). The morphants showed gross morphological defects, cardiac edema, and severe anteroposterior axis defects in the larval stages as well (Fig. 1SE). The phenotypes were observed in a morpholino dose-dependent manner (Fig. S1C). Similar phenotypes were obtained with the cep57 splice blocker morpholino as well (Fig. 1F). To ascertain the specificity of the

morpholinos, we performed rescue experiments by co-injecting the zCep57 mRNA and splice blocker morpholino at 1-cell stage embryos. The co-injection of cep57 mRNA significantly rescued all the phenotypes (Fig. 1F, S1D).

### *cep57* plays a key role in neural crest specification and mesodermal patterning

As the *cep57* morphants showed structural and architectural defects in the neural tissue (Fig. 1G), we examined the morphants for cranial neural crest specification and patterning. We determined the spatio-temporal expression patterns of cranial neural crest specifiers *crestin*, *twist1a,* and *sox10* in the *cep57* morphants. *Crestin* is a pan-neural crest marker, expressed in premigratory and migrating neural crest cells.[17] *Twist1a* and *sox10* are expressed in the premigratory cranial neural crest cells and are required for neural crest survival, specification, and migration.[18] We observed severe down-regulation of *crestin*, *twist1a,* and *sox10* in the *cep57* morphants at the early somitogenesis phase (red asterisk, Fig.2A, B, C) and 24hpf P2 morphants (double red asterisk, Fig. 2D, E, F). The down-regulation of these specifier genes strongly suggests that *cep57* is essential to maintain the neural crest progenitor fate. Also, *sox2* is essential for the proliferation and maintenance of neural progenitors.[18–20] The *cep57* morphants showed a severe downregulation of sox2 (red asterisk, Fig. 2G) and notochordal defects marked by *tbxta* expression in the *cep57* morphants (red arrow, Fig. 2H).[18,21] The midbrain-hindbrain architecture remained unchanged upon cep57 depletion, as shown by *pax2a* and *egr2b* expression patterns (Fig. S2A, B). However, the morphants showed defects in somite architecture and organization, as marked by *myoD1* expression (red arrow, Fig. S2C).

### *cep57* depletion results in a microcephaly-like phenotype

The post-migratory cranial neural crest gives rise to the head mesenchyme, cartilage, and skeletal craniofacial elements.[22,23] As *cep57* depletion resulted in the reduced expression of cranial neural crest specifiers (Fig. 2), we examined the craniofacial skeletal organization in *cep57* morphants at the larval stage (Fig. 3A). The *cep57* P1 and P2 morphants showed severe craniofacial dysmorphic features, cartilage, and skeletal abnormalities at larval stages (red asterisk, Fig. 3A). These defects can be attributed to the reduced expression of neural crest specifier genes like

*sox10*, as the craniofacial skeletal elements primarily develop from neural crest-derived mesenchyme.[18,22,23] The *cep57* larvae exhibited reduced head size and interpupillary distance (IPD) (Fig. 3B), indicative of a microcephaly-like phenotype. Interestingly, we observed a downregulation of microcephaly-associated genes *mcph1, wdr62, ankle2, map11, kif14*, and *aspm* (Fig. 3C). *Mcph1* regulates centrosome dynamics and entry into the M phase in murine neural progenitor cells.[24] The depletion of MCPH1 induces precocious entry into the M phase, premature chromosome condensation, and misalignment. In the brain, MCPH knockdown results in reduced neuroprogenitor cells and, thus, a reduced number of neurons. [25] *Wdr62, map11,* and *kif14* are known to regulate key events of mitosis in neural progenitor cells, such as stabilizing spindle poles, organization of the mitotic spindle, and cytokinesis.[25,26] *Ankle2, wdr62,* and *aspm* are essential for the maintenance of the progenitor population, regulating the differentiation of progenitors and, consequently, overall brain size.[25,27–30] The reduced expression of these microcephaly markers shows that *cep57* plays a key role in the maintenance of neural progenitor cell fate and regulating head size.

**Cep57 is essential for cell cycle progression, and its depletion results in G1 arrest**

To further probe the cellular basis of microcephaly-like phenotype, we examined the extent of cell death in *cep57* morphants. Indeed, the *cep57* morphants showed embryo-wide apoptosis in the head, trunk, and tail, as shown by acridine orange staining (red asterisks, Fig. 4A). The cell death observed in the *cep57* morphants may be the result of aberrant DNA damage response and or centrosome-based mitotic aberrations. Many MCPH genes like *mcph1* and *cep152* have been implicated in both centrosomal and DNA damage responses.[31] Hence, we used a random amplified polymorphic DNA (RAPD) PCR assay to check for genomic instability, DNA alterations, damage, and mutations. [32,33] The amplification products obtained showed many bands of molecular size between 300 to 1500bp (arrows, Fig. 4B). The *cep57* morphants showed variation in band intensity as well as loss of polymorphic bands in the amplification patterns with respect to control (red arrows, Fig. 4B). We observed that the disappearance of bands in *cep57* morphants suggests a reduction in genomic stability with a 38.7% reduction in genomic template stability (GTS%) (Fig. 4B). [32,33] DNA damage response is also mediated by Rad21, a core cohesin complex member that enables the separation of sister chromatids. The depletion of

Rad21 results in impaired DNA damage response and is critical for DNA damage repair. In addition to proteolytic cleavage during mitosis, it is also cleaved during nuclear fragmentation in apoptosis.[34,35] The morphants showed depletion of Rad21 protein, indicating abrogation of DNA damage response upon *cep57* depletion (Fig. 4C).

Besides DNA damage and increased apoptosis in the neural progenitor cells, the development of microcephaly can be attributed to checkpoint defects and mitotic errors. In fact, DNA damage also activates cell cycle checkpoints, and the cell undergoes growth arrest to repair damaged DNA before S phase (G1 arrest) or before M phase (G2 arrest).[36] We examined the *cep57* morphants for cell cycle progression and checkpoint regulators (Fig. 4D-H). Fluorescence-based flow cytometry analysis revealed a significant increase in the G1 phase and concomitant reduction in the G2/M phase in the *cep57* morphants from control (Fig. 4D, E). The cep57 morphants showed reduced PH3 staining, indicating a reduction in M phase cells (Fig. 3B). The S phase remained unchanged in the morphants (Fig. 4E). The whole embryo DNA content flow cytometry assay was validated by western blotting for cell cycle markers (Fig. 4F, G). Geminin is one of the master regulators of cell cycle progression, accumulating in S, G2, and M phases.[37] At G1, geminin levels are low; during G1-S transition, geminin accumulates to initiate DNA replication. High levels of geminin in the G2 and M phase ensure that DNA re-replication is inhibited. At metaphase-anaphase transition, geminin is degraded to prepare the cell for the next cycle. [38,39] Ectopic expression of Geminin in G1 elicits cell cycle arrest, failure to progress into S phase, and apoptosis. [40] The *cep57* morphants showed an upregulation of geminin, validating the G1 arrest and apoptosis phenotype (Fig. 4F). Progression throughout the cell cycle requires the regulatory oscillatory activity of cyclins and cyclin-dependent kinases (CDKs). Cyclin-dependent kinase 1 (CDK1) regulates G1 to S and G2 to M phases, and its activity is modulated by phosphorylation and binding to Cyclin B1.[41] CDK1 levels are low in G1, and activity increases by late G1 until anaphase. The *cep57* morphants showed an upregulation of Cdk1 levels, indicating G1 arrest (Fig. 4G). The DNA damage-induced G1 to S kinase, Cyclin E levels increased in the morphants, which also results in G1 arrest (Fig. S3A). The MAPK kinases MEK1/2 and ERK1/2 cascade also play an important role in cell cycle progression and mitosis. Mek1/2 depletion results in G1 arrest, increased p21 levels, and induction of apoptosis.[42] The cep57 morphants also showed depleted levels of Mek1 (Fig. 4G). The depletion of Mek1 also results in notochordal defects during somitogenesis in zebrafish.[43] Hence, the notochordal

defects seen in cep57 morphants may also be attributed to reduced Mek1 levels. We also observed an upregulation of CDK inhibitors *p21* and *p27* transcripts, which in turn inhibit CDK2 and attributing to the cep57-induced G1 arrest (Fig.4H).[44] *p21* over-expression also leads to abnormal mitosis.[36] These results show that *cep57* modulates the cell cycle through transcriptional regulation as well. Hence, *cep57* plays a crucial role in cell cycle progression, and its depletion results in G1 arrest. The G1 arrested cells can either undergo repair or apoptosis.[44] In *cep57* morphants, the progenitor cells most likely undergo the apoptotic pathway, resulting in a smaller head size and microcephaly-associated features.

**Cep57 maintains spindle pole integrity during embryonic mitoses and proteome profiling of *cep57* morphants**

As Cep57 localizes to the centrosomes in zebrafish blastulae, we investigated the role of *cep57* in centrosomal and mitotic progression. The *cep57* morphants showed reduced *kif14* and *aspm* levels (Fig.3C), which also allude to impaired mitotic progression and anomalies.[25,29,45–47] We thus examined the morphants for mitotic aberrations during early embryonic divisions (Fig. 5A, B). The morphants showed spindle pole focusing defects (red asterisks, Fig.5A, B, C), highlighting the centrosomal function of *cep57* in maintaining spindle pole integrity, in a manner akin to Xenopus egg extract system.[7] Aberrations in spindle pole focusing can result in the unequal distribution of chromosomes, genomic instability, and cell death.[48] To probe further into the mechanistic basis of the *cep57* knockdown phenotypes, we performed label-free LC-MS/MS proteomics analysis to identify differentially regulated proteins in *cep57* morphants (Fig. 5D, E). The resultant peptides were mapped to the *Danio rerio* Uniprot database, and the results were exported to a Microsoft Excel table, including data for protein abundances, number of peptides, protein coverage and search identification score, etc. ID mapping was performed using Uniprot, and Gene Ontology (GO) term analysis was performed using ShinyGO 0.76.2.[49,50] Proteins with FDR<0.01 were qualified for quantification with a fold change cutoff ratio (FC) of >2.0 or <0.5 set as the threshold to identify differentially expressed proteins. We confidently identified 116 upregulated and 55 downregulated proteins in the *cep57* morphants (Fig. S4, S5). Owing to the limited mapping of zebrafish proteome in multiple databases such as Panther, String, and ShinyGo, a total of 19 GO terms were identified, including biological processes (Fig. S3C) for

the upregulated category and a total of 18 GO terms, including molecular function (Fig. S3D) for the downregulated proteins. The GO terms of the fold-enriched biological processes were apoptosis, microtubule dynamics, vesicular trafficking, and cytoskeletal organization in the upregulated protein category (Fig. 5E). For downregulated proteins, the GO terms for fold-enriched biological processes were chromosome condensation, sister chromatid cohesion, and segregation coupled with cell cycle regulators (Fig. 5D). Hence, gene ontology analysis corroborates our results to show that *cep57* depletion results in chromatid-associated defects and increased apoptosis-promoting factors, resulting in impaired cell cycle progression and a surge of apoptosis.

The comparative proteome analysis showed many interesting leads into Cep57 molecular functions. Consistent with our experiments showing DNA damage and increased apoptosis upon *cep57* depletion, the comparative proteome also revealed upregulation of pro-apoptotic proteins such as AnnexinV, Arid3B, Cpped1, Pp2A, and Dapk1 (yellow highlights, Fig.S4). ANNEXIN V is a marker for apoptosis as it binds to phospatidylserine, which translocates to the cell surface in apoptotic cells.[51–53] ARID3B activates pro-apoptotic p53 target genes and induces apoptosis.[54] The overexpression of CPPED1 results in impaired cell cycle progression and promotes apoptosis.[55] Protein phosphatase 2A (PP2A) upregulation leads to caspase 3 activation and hence has a pro-apoptotic function.[56] Death-associated protein Kinase 1 (DAPK1) is a key regulator of cell death and mediates caspase-dependent and caspase-independent pro-apoptotic signaling. Recent reports also show its function in tumor suppression and neuronal cell death.[57–59] Interestingly, the cep57 depleted proteome showed upregulation of cytoplasmic Dynein intermediate chain 1 gene, which is a sensenscence-associated gene, and its upregulation is correlated with cell cycle arrest and cellular senenscence.[60] Thus, proteome profiling strongly suggests that *cep57* is essential for cell survival during early embryogenesis.

In cycling cells, normal cell cycle progression is critical for genome stability and integrity. The cell cycle checkpoints at G1/S, G2/M, and M/G1 ensure that each phase is completed without errors. 14-3-3 Proteins function at G1/S transitions and regulate the timing of mitosis. They interact with the CDK inhibitor p27, which mediates G1 arrest. In G1-arrested cells, depletion of 14-3-3 results in cell death.[61,62] The *cep57* morphants exhibiting DNA damage and G1 arrest showed downregulation of 14-3-3 protein (orange highlights, Fig. S5), indicating mitotic

catastrophe and, hence, apoptosis. During the G1/S phase, the cohesin complex, which holds the newly synthesized sister chromatids, is loaded onto the chromatin. Aberrations in the cohesin complex result in premature separation of sister chromatids before anaphase and cell death. CTF8 is essential for the establishment of sister chromatid cohesion, and its depletion results in cohesion defects, chromosome segregation defects, and cell cycle arrest.[63,64] Our proteome data shows downregulation of CTF8, indicative of impaired cell cycle progression and cell death (orange highlights, Fig. S5). We also observed decreased Smc4 levels in cep57 morphants (orange highlights, Fig. S5). Smc4 is part of the condensin complex, and its phosphorylation induces G1 arrest and plays a key role in single-strand DNA break repair.[65–67] The comparative proteome data also showed a downregulation of Cyclin-dependent kinase 7 (CDK7) in *cep57* morphant embryos (orange highlights, Fig. S5). CDK7 phosphorylates CDK4 and CDK6 to initiate G1 progression and CDK2 for G1/S transition. The G2/M transition is also induced by CDK7 mediated phosphorylation of CDK1. Mice lacking CDK7 showed increased apoptosis, and it is essential for neural progenitor proliferation.[68] CDK7 depletion results in decreased phosphorylation of CDK1 and CDK2, resulting in G1/S arrest. CDK7 inhibition also results in BAK and caspase 3/8 activation. It also upregulates AnnexinV in the G1 phase, promoting apoptosis. [69–71] In summary, quantitative mass spectrometry-based proteome profiling of control and *cep57* morphants revealed a differential proteome of cell cycle progression and apoptosis-associated proteins, which provide fresh mechanistic insights into *cep57*-mediated cellular functions.

**Discussion:**

Centrosomal aberrations, genome instability, and aneuploidy are often associated with microcephaly. Microcephaly is attributed to the failure of self-renewal or DNA damage in neural progenitor cells owing to checkpoint defects, DNA repair deficiencies, mitotic errors, and increased apoptosis. Thus, the crosstalk between DNA damage response and centrosome is critical to understand the basis of microcephaly. Many genes, such as *mcph1* and *cep152*, are shown to have DNA damage response and centrosomal functions.[31] Here, we show that Cep57 localizes to the centrosomes and nucleus during early embryogenesis. *Cep57* depletion results in G1 arrest and spindle pole focusing defects at metaphase (Fig. 6A). The *cep57* morphants showed neurodevelopmental defects, increased apoptosis in the neural progenitors, decreased

expression of neural crest specifier genes, and microcephaly-associated features (Fig. 6B). The comparative proteome analysis highlights previously unexplored *cep57* mediated regulation of G1 arrest and DNA damage inducing proteins such as Dapk1, Arid3B, Cpped1, Pp2a, and AnnexinV and cell cycle modulators such as Smc4, 14-3-3, Ctf8, and CDK7 (Fig. 6A). Here, we uncover previously unknown functions of *cep57* in cell cycle progression, spindle pole integrity, and cranial neural crest specification during early vertebrate embryogenesis. Hence, the *cep57* mediated microcephaly phenotype may be attributed to impaired cell cycle progression, G1 arrest, and increased apoptosis. However, our study has certain limitations. As we have investigated the cellular and developmental functions in an *in vivo* animal model-based knockdown system, we have not ruled out the contributions due to functional redundancy, particularly in regulating mitotic events with other *cep* family members. Also, we obtained a limited number of proteins in the quantitative proteome analysis due to restrained proteome mapping of zebrafish proteins to publicly available databases. Yet, the *cep57* microcephaly model can be used to study the mechanistic basis of MVA-associated microcephaly. Future experiments to investigate *cep57* functions in spindle assembly checkpoint, microtubule stability, and chromosome integrity will be imperative to uncover its diverse mitotic functions.

## Methods:

### Zebrafish lines, MO injection, and characterization of phenotypes

Tubingen strain (TU-AB) zebrafish were raised according to standard protocols as described earlier. All experiments were performed according to protocols approved by the Institutional Animal Ethics Committee of the Council of Scientific and Industrial Research, Centre for Cellular and Molecular Biology, India. Embryos were obtained from the natural spawning of adult fish, kept at 28.5°C, and staged according to hours after fertilization. [72] The endogenous *cep57* levels were depleted by using MO *cep57* translation blocker, 5'-AGGCTTTTGAGTTCGTCTCCATTAA-3′ and cep57 splice blocker, 5'-TGTCATAATGGACTCACAAGCTCAT-3' (Gene Tools). For rescue experiments, cep57 mRNA was *in vitro* transcribed (AM1340, Thermo Scientific), and 50pg of mRNA was co-injected along with c*ep57* splice MO in each embryo at the one-cell stage. The embryos were then analyzed for gross morphological defects and survival at later stages of development (till 5dpf) and were imaged in Zeiss Stemi508 stereomicroscope.

### Antisense riboprobe preparation

For cloning sequence-specific exonic fragments to synthesize riboprobes, total RNA was isolated from a pool of 100 embryos (24hpf) of the TU-AB strain using an RNA isolation kit (MN; 740955.50). The total RNA was used to prepare cDNA using the PrimeScript 1$^{st}$ strand cDNA synthesis kit (TaKaRa, Cat. # 6110A). Sequence-specific primers were used to amplify the specific gene fragment and cloned into the pGEMT easy vector, and the sequence was verified. The sequence-verified plasmid was linearised using Nco1, and antisense digoxigenin (DIG)-labeled riboprobes were synthesized using the DIG RNA labeling kit (Roche #11175025910). [18]

### Whole Mount RNA in Situ Hybridization

The control and the morphant embryos of the desired developmental stage were dechorinated and fixed in 4% paraformaldehyde (PFA) in PBS overnight. The embryos were then washed with PBT (1× PBS and 0.1% Tween 20) and stored in methanol at -20 $^{0}$C overnight. Embryos were rehydrated using decreasing gradation of Methanol-PBT followed by pre-warmed hybridization wash buffer (50% formamide, 1.3 × SSC, 5 mM EDTA, 0.2%, Tween-20) and blocking in pre-warmed hybridization mix buffer (50% formamide, 1.3 × SSC, 5 mM EDTA,

0.2%, Tween-20, 50 μg/mL yeast t RNA, 100 μg/mL heparin) for 5 hours at 55 $^{0}$C. DIG labelled RNA probe was added (1ng/ul) and kept overnight at 55 $^{0}$C. The next day the embryos were washed with a prewarmed hybridization mix buffer followed by washes of gradation of 2X SSC (20X SSC stock-3M NaCl, 0.3M sodium citrate, pH7.2), Hybridization wash buffer, 0.2XSSC and TBST (0.5 M NaCl, 0.1 M KCl, 0.1 M Tris, pH 7.5 and 0.1% Tween 20) at room temperature. The embryos were then given a TBST wash and then blocked in 10% heat inactivated fetal bovine serum (Gibco; 16210-064) in TBST for 3 hours at room temperature. Anti-DIG antibody (1:5000) was added and incubated overnight at 4°C. Next day, four washes of TBST were given at room temperature followed by four washes of NTMT (0.1M NaCl, 0.1 M Tris-Cl at pH 9.5, 0.05M MgCl2, 1% Tween-20) and stained with 1-step NBT/BCIP solution (Thermo scientific, cat. no. 34042). Fresh NTMT was added to stop the reaction for both control and morphant embryos simultaneously and photographed using Zeiss Stemi508 stereomicroscope and Zeiss AxioZoom V16 microscope.[18]

**RNA isolation, semi-quantitative PCR**

Total RNA was isolated from 100 embryos for each group using the RNA isolation kit (MN; 740955.50) as per the manufacturer's protocol. Quantitative real-time PCR (qPCR) was setup in ViiA7 Real-Time PCR System (Applied Biosystems) using the prepared cDNA as a template along with PowerSYBR Green PCR master mix (Applied Biosystems, cat. no. 4367659) and the following program was used: 40 cycles of 95 $^{0}$C -10min., 95 $^{0}$C -15 sec., 60 $^{0}$C -1 min., 95 $^{0}$C -15 sec., 60 $^{0}$C -1 min., 95 $^{0}$C -15 sec. Zebrafish *β-actin* was used as an internal control. The gene expression levels were measured in triplicates for control and morphants. The fold change of the genes tested was calculated using the $2^{-\Delta\Delta Ct}$ (the delta-delta-Ct) method. All primers used in this study are listed in Fig.S6.

**Acridine orange staining**

Acridine orange (AO) staining was performed to detect the apoptotic cells in 1dpf embryos. The control and morphant embryos were dechorinated, stained with 5mg/L AO for 1 hour in the dark, and then washed with embryo water. The embryos were anesthetized with tricaine, and the bright green dots in the embryos indicated apoptotic cells. The number of apoptotic cells in the

head region was counted using Image J software. The apoptotic cells in the embryos were photographed by Zeiss AxioZoom V16 microscope.[18,73]

**Skeletal preparations - Alcian blue and Alizarin red staining**

Five day-old control and morphants larvae were fixed in 4% PFA/PBS overnight at $4^0$C. The embryos were washed with 1XPBS and stored in methanol at -20 $^0$C overnight. The staining solutions needed for bone and cartilage staining were prepared: Solution A (0.04% Alcian blue, 125mM MgCl2, 70% ethanol) and Solution B (1.5% Alizarin Red S). 1 ml of solution A and 20ul of solution B were added to the larvae and kept overnight at room temperature in dark with constant rocking. The staining solution was removed, and the larvae were washed twice with water. Then, embryos were then transferred to bleach solution (1% KOH, 1.5% $H_2O_2$) for 1 hour at room temperature followed by a gradation of Glycerol-KOH washes. The embryos were then stored in 50% glycerol-0.25% KOH, and the larvae were imaged using Zeiss AxioZoom V16 microscope. For microcephaly analysis of the 5dpf larvae, the interpupillary distance (IPD) and the head size defined by the otic vesicle and the semicircle of eyes as posterior and lower boundary were quantified using Image J software.[74]

**Western Blot analysis**

Lysates of embryos younger than 1dpf were prepared by homogenizing approximately 100 embryos using RIPA buffer (20mM Tris–HCl, pH 7.4; 150mM NaCl; 5mM EDTA; 1% NP-40; 0.4% sodium deoxycholate, 0.1% SDS and 1× Protease inhibitor cocktail). The lysis was carried by incubating on ice for 15 minutes with intermittent vortexing. The homogenized lysates were centrifuged (12000 rpm for 20 min at 4°C), and supernatants were collected. The samples were then boiled in Laemmli buffer at $95^0$C for 10 mins. For 1dpf embryos, the embryos were first dechorinated and then deyolked by gentle pipetting using deyolking buffer (55mM NaCl, 1.8mM KCl, 1.25mM $NaHCO_3$) followed by centrifugation at 3000rpm for 30secs. The embryos were then washed using wash buffer (110mM NaCl, 3.5mM KCl, 2.7mM $CaCl_2$, 10mM Tris HCl, pH8.5), centrifuged at low speed, and the supernatant was discarded. The pellet was then boiled in Laemmli buffer at $95^0$C for 10 mins. 20 µg of total protein was loaded in each lane and run on a 10% SDS-PAGE gel using Tris-Glycine SDS buffer for the detection of endogenous proteins. Proteins were then transferred to methanol-activated PVDF membranes (Merck Millipore,

ISEQ00010) by electro-blotting. The membranes were then blocked either in 5% non-fat dry milk (sc-2324) or 5% BSA (Bovine serum albumin, for phosphoproteins) prepared in TBST (20 mM Tris HCl, pH 7.5, 150 mM NaCl, 0.05% Tween 20) for 1 hour. The blots were probed with primary antibody prepared in 1% blocking solution for 14-16 hours at $4^0$C. The blots were then washed with 1X TBST three times and incubated with HRP-conjugated secondary antibody for 1 hr. The blots were then washed again three times with TBST and developed for chemiluminescence signal using the chemiluminescent substrate (Thermo scientific- 34577) and captured in the Vilber-Lourmat Chemiluminescence System. The primary and secondary antibodies used in this study are listed in Fig.S6.

**Immunohistochemistry of zebrafish embryos**

The control and morphant embryos at the 256-cell stage were fixed in 4% PFA/PBS at $4^0$C overnight, followed by methanol fixation. The methanol-fixed embryos were rehydrated with 50% MeOH/PBS followed by PBS washes and then blocked in 1% BSA/PBST (1X PBS and 0.1% Triton X-100) for 2 hours at room temperature. The embryos were then incubated with primary antibody, prepared in blocking solution overnight at 4 °C. PBST washes were given followed by incubation with appropriate secondary antibody overnight at 4 °C. The embryos were again washed with PBST, and DAPI (1µg/ml) was added for 10min, washed with 1X PBS, and stored at -20 °C until imaging. The image acquisition was done using Leics TCS SP8 confocal microscope. The mitotic phenotypes were quantified using 3D reconstruction of the confocal images using the IMARIS software. The primary and secondary antibodies used in this study are listed in Fig.S7.

**Nuclear cytoplasmic fractionation**

200 wild-type 24 hpf embryos were taken, dechorinated, and deyolked. Ice-cold 0.1% NP40 prepared in PBS was added and gently pipetted 5-10 times. 200ul of lysate was removed as the whole embryonic lysate. The remaining sample was centrifuged at 2000 rpm for 5 minutes. The supernantant was carefully collected as the cytoplasmic fraction. To the pellet, ice-cold 0.1% NP0/PBS was added, and gentle pipetting was done. The sample was again centrifuged, and the supernantant was discarded. The pellet contains the nuclear fraction. Laemmli buffer was added

to all the three fractions, properly lysed, and heated at $95^0$C for 10 mins. The fractions were confirmed by probing with GAPDH (cytoplasmic marker) and LAMIN B1 (nuclear marker)[75]

**Genomic DNA isolation and RAPD PCR**

Genomic DNA isolation was done for both control and morphant embryos using the Macherey-Nagel nucleospin tissue kit as per the manufacturer's protocol. PCR reaction was set up using primer with sequence 5'-CCCGTCAGCA-3' and the isolated DNA(200ng) as a template for 25cycles. The PCR products were run on 2% agarose gel and visualized under UV light. The difference in the PCR profiles of control and morphants forms the basis of the genomic template stability (GTS). GTS= (1-a/n)*100, where a is the number of polymorphic bands in morphants and n is the total number of bands in control. GTS is expressed as a percentage with control set to 100%. [76]

**Whole embryo DNA content FACS-based cell cycle analysis**

24hpf control and morphant embryos were dechorinated, deyolked, and centrifuged at 3000rpm for 30secs. To obtain a single cell suspension, PBS was added to the pellet, and the cells were disintegrated using a 24-gauge syringe. The single-cell suspension was then centrifuged at 1000rpm for 2mins at $4^0$C. The pellet was discarded, and the supernatant was collected in a fresh Eppendorf tube and centrifuged at 1500 rpm for 15 mins at $4^0$C. The supernatant was discarded, and the pellet was resuspended in DAPI (10ug/ml) prepared in PBS. The single cell suspension was then centrifuged at 1500rpm for 15mins at $4^0$C, resuspended in PBS, and used for flow cytometry analysis using Beckman Coulter Gallios. 300000 singlet events were calculated for both control and morphants for cell cycle analysis. The data was analysed using Kaluza Analysis 2.2 software, and plots were obtained with the histogram of the linear DAPI area using the J.V. Watson algorithm.

**Label-free quantification and proteome analysis**

For comparing the changes in the total proteome upon gene knockdown, label-free quantification was done using mass spectrometry. Lysates of 24hpf control and *cep57* morphant embryos were prepared using RIPA buffer. 100ug of total protein of each sample was separated on 10% SDS-PAGE gel. The gel was stained using Coomassie blue and destained with acetic acid and

methanol. The protein-loaded lane was excised from the gel and fragmented into multiple pieces. The gel pieces were then alternately washed with 50 mM ammonium bicarbonate and acetonitrile to clear off the Coomassie blue stain from the gel pieces. Further, the gel pieces were subjected to reduction reaction using 10mM dithiothreitol followed by alkylation using 55mM iodoacetamide. In-gel trypsin digestion was carried out at $37^0$C for 16 hours. The peptides were extracted using an extraction buffer (5% formic acid, 30% acetonitrile) and desalted using C18 reversed phase material-bound Zip Tips. The peptides were analyzed using the Thermo Scientific Easy-nLC 1200 system coupled to Q-Exactive mass spectrometer (Thermo Scientific). The peptides were resolved on a Thermo Scientific PepMap RSLC C18, 3µm, 100 A, 75 µm x 15 cm column (ES900) using a 5% - 25% - 45% - 95% -95%-3% Solvent B gradient followed at 0.00, 35.00, 41.00, 46.00, 49.00, 53.00 and 60.00 minutes respectively, (Solvent A: 5% acetonitrile - 0.2% formic acid; Solvent B: 90% acetonitrile - 0.2% formic acid), in DDA mode (data dependent mode). The nLC eluent was sprayed into the QE with a spray voltage of 2.2Kv (kilovolts). The mass spectrometer was operated in the positive ion mode, and the settings with MS1 scans ranged over 400 – 1650 m/z, with AGC target, $3e^6$, resolution 70000. MS2 scans ranged over 200-2000m/z and resolution 17500. The data was acquired with the following set parameters: normalised collision energy 30, topN 10 peptides with charge exclusion 1, 6-8 and >8. The data was analysed using the Proteome Discoverer 2.2 software (Thermo Scientific), and the proteins were identified by performing a search against the *Danio rerio* Uniprot database (UP000000437). SEQUEST HT algorithm was used along with other analysis parameters such as trypsin enzyme specificity, carbamidomethyl static modification, mass tolerance set to 10ppm, and fragmentation tolerance set to 0.02 Da. Normalization mode was used for the total peptide amount along with pairwise ratio-based calculation. The percolator algorithm was used to validate peptide spectral matches (PSM), and a q-value cutoff of 0.01 (1% global False Discovery Rate, FDR) was used for proteome mapping, fold change, and GO analysis. Gene ontology enrichment analysis was performed using the ShinyGO database.

**Statistical analysis**

Each experiment was repeated a minimum of three times independently. GraphPad Prism software was used for all statistical analyses. All the values are shown as mean with SEM unless

specified. Data were analysed using unpaired *t-test* for statistical significance. A *P* value less than 0.05 was considered statistically significant.

**Data availability**

The mass spectrometry proteomics data have been deposited to the ProteomeXchange Consortium via the PRIDE [1] partner repository with the dataset identifier PXD062612.[77]

**CRediT authorship contribution statement**

Conceptualization: MK, Methodology: SI and MK, Validation: SI and MK, Formal analysis: SI and MK, Investigation: SI, PSM, AG and MK, Resources: MK, Data curation: SI and MK, Writing – original draft: SI and MK, Writing – review and editing: SI and MK, Visualization: SI and MK, Supervision: MK, Project administration: MK, Funding acquisition: MK

**Declaration of competing interest**

The authors have no competing interests.

**Acknowledgments**

We sincerely thank Mr. G. Srinivas, Advanced microscopy & cell sorting facility, and Mr. B. Raman, Ms. Y. Kameshwari, and Mr. K. Ranjith Kumar, Proteomics facility, CSIR-CCMB, for their assistance with the experiments. SI acknowledges CSIR, India, for the research fellowship. MK thanks the Council of Scientific and Industrial Research - Centre for Cellular and Molecular Biology (CSIR-CCMB), Govt. of India, and the Department of Science and Technology (DST), Govt. of India (DST/INSPIRE/04/2016/001436) for supporting and funding this research.

**References:**


1. De la Torre-García, O. *et al.* A homozygous CEP57 c.915_925dupCAATGTTCAGC mutation in a patient with mosaic variegated aneuploidy syndrome with rhizomelic shortening in the upper and lower limbs and a narrow thorax. *Eur. J. Med. Genet.* **62**, 195–197 (2019).

2. Watanabe, K., Takao, D., Ito, K. K., Takahashi, M. & Kitagawa, D. The Cep57-pericentrin module organizes PCM expansion and centriole engagement. *Nat. Commun.* **10**, (2019).

3. Ito, K. K. *et al.* Cep57 and Cep57L1 maintain centriole engagement in interphase to ensure centriole duplication cycle. *J. Cell Biol.* **220**, (2021).

4. Aziz, K. *et al.* Mosaic-variegated aneuploidy syndrome mutation or haploinsufficiency in Cep57 impairs tumor suppression. *J. Clin. Invest.* **128**, 3517–3534 (2018).

5. Zhao, H. *et al.* Cep57 and Cep57l1 function redundantly to recruit the Cep63-Cep152 complex for centriole biogenesis. *J. Cell Sci.* **133**, (2020).

6. Lukinavičius, G. *et al.* Selective chemical crosslinking reveals a Cep57-Cep63-Cep152 centrosomal complex. *Curr. Biol.* **23**, 265–270 (2013).

7. Emanuele, M. J. & Stukenberg, P. T. Xenopus Cep57 Is a Novel Kinetochore Component Involved in Microtubule Attachment. *Cell* **130**, 893–905 (2007).

8. Snape, K. *et al.* Mutations in CEP57 cause mosaic variegated aneuploidy syndrome. *Nat. Genet.* **43**, 527–529 (2011).

9. Sukla, S. *et al.* Crystal structure of human Cep57 C-terminal domain reveals the presence of leucine zipper and the potential microtubule binding region. *Proteins Struct. Funct. Bioinforma.* **92**, 1137–1143 (2024).

10. Wu, Q. *et al.* Cep57, a NEDD1-binding pericentriolar material component, is essential for spindle pole integrity. *Cell Res.* **22**, 1390–1401 (2012).

11. Zhou, H., Wang, T., Zheng, T., Teng, J. & Chen, J. Cep57 is a Mis12-interacting kinetochore protein involved in kinetochore targeting of Mad1-Mad2. *Nat. Commun.* **7**, 1–13 (2016).

12. He, R. *et al.* Cep57 protein is required for cytokinesis by facilitating central spindle microtubule organization. *J. Biol. Chem.* **288**, 14384–14390 (2013).

13. Langeh, N. *et al.* Mosaic variegated aneuploidy syndrome 2 with biallelic novel CEP57 splice site variation in Indian siblings: Expanding the clinical and molecular spectrum. *Clin. Genet.* **103**, 478–483 (2023).

14. Feng, B. *et al.* A novel CEP57 variant associated with mosaic variegated aneuploidy syndrome in a Chinese female presenting with short stature, microcephaly, brachydactyly, and small teeth. *Mol. Genet. Genomic Med.* **10**, 1–7 (2022).

15. Santos-Simarro, F. *et al.* Mosaic Variegated Aneuploidy syndrome 2 caused by biallelic variants in CEP57, two new cases and review of the phenotype. *Eur. J. Med. Genet.* **64**, 1–

7 (2021).

16. Pinson, L. *et al.* CEP57 mutation in a girl with mosaic variegated aneuploidy syndrome. *Am. J. Med. Genet. Part A* **164**, 177–181 (2014).

17. Luo, R., An, M., Arduini, B. L. & Henion, P. D. Specific pan-neural crest expression of zebrafish crestin throughout embryonic development. *Dev. Dyn.* **220**, 169–174 (2001).

18. Iyer, S. *et al.* Exposure to Tetrabutylammonium Bromide Impairs Cranial Neural Crest Specification, Neurogenic Program, and Brain Morphogenesis. *ACS Chem. Neurosci.* **14**, 1785–1798 (2023).

19. Gou, Y., Guo, J., Maulding, K. & Riley, B. B. Sox2 and Sox3 Cooperate To Regulate Otic/Epibranchial Placode Induction in Zebrafish. *Dev. Biol.* **435**, 84–95 (2018).

20. Germanà, A. *et al.* Developmental changes in the expression of Sox2 in the zebrafish brain. *Microsc. Res. Tech.* **74**, 347–354 (2011).

21. Schulte-Merker, S., Van Eeden, F. J. M., Halpern, M. E., Kimmel, C. B. & Nüsslein-Volhard, C. no tail (ntl) is the zebrafish homologue of the mouse T (Brachyury) gene. *Development* **120**, 1009–1015 (1994).

22. Dutton, K. A. *et al.* ectomesenchymal neural crest fates □. 1–8 (2001).

23. Honoré, S. M., Aybar, M. J. & Mayor, R. Sox10 is required for the early development of the prospective neural crest in Xenopus embryos. *Dev. Biol.* **260**, 79–96 (2003).

24. Journiac, N. *et al.* Cell Metabolic Alterations due to Mcph1 Mutation in Microcephaly. *Cell Rep.* **31**, (2020).

25. Overview, A. brain sciences Molecular Genetics of Microcephaly Primary Hereditary□: *Nikistratos Siskos , Electra Stylianopoulou , Georg. Skavdis Maria E. Grigoriou, Electra Stylianopoulou , Georg. Skavdis Maria E. Grigoriou* (2021).

26. Perez, Y. *et al.* Mutations in the microtubule-associated protein MAP11 (C7orf43) cause microcephaly in humans and zebrafish. *Brain* **142**, 574–585 (2019).

27. Xu, D., Zhang, F., Wang, Y., Sun, Y. & Xu, Z. Microcephaly-associated protein WDR62 regulates neurogenesis through JNK1 in the developing neocortex. *Cell Rep.* **6**, 104–116 (2014).

28. Apridita Sebastian, W. *et al.* Ankle2 deficiency-associated microcephaly and spermatogenesis defects in zebrafish are alleviated by heterozygous deletion of vrk1. *Biochem. Biophys. Res. Commun.* **624**, 95–101 (2022).

29. Kim, H. T. *et al.* The microcephaly gene aspm is involved in brain development in zebrafish. *Biochem. Biophys. Res. Commun.* **409**, 640–644 (2011).

30. Novorol, C. *et al.* Microcephaly models in the developing zebrafish retinal neuroepithelium point to an underlying defect in metaphase progression. *Open Biol.* **3**, 130065 (2013).

31. Marjanović, M. *et al.* cep63 Reveals a Role for the Centrosome in Meiotic

Recombination. *Nat. Commun.* (2016) doi:10.1038/ncomms8676.CEP63.

32. Atienzar, F. A., Venier, P., Jha, A. N. & Depledge, M. H. Evaluation of the random amplified polymorphic DNA (RAPD) assay for the detection of DNA damage and mutations. *Mutat. Res. - Genet. Toxicol. Environ. Mutagen.* **521**, 151–163 (2002).

33. Zhiyi, R. & Haowen, Y. A method for genotoxicity detection using random amplified polymorphism DNA with Danio rerio. *Ecotoxicol. Environ. Saf.* **58**, 96–103 (2004).

34. Idilli, A. I., Pazzi, C., Dal Pozzolo, F., Roccuzzo, M. & Mione, M. C. Rad21 haploinsufficiency prevents ALT-associated phenotypes in zebrafish brain tumors. *Genes (Basel).* **11**, 1–14 (2020).

35. Cheng, H., Zhang, N. & Pati, D. Cohesin subunit RAD21: From biology to disease. *Gene* **758**, 144966 (2020).

36. Blagosklonny, M. V. & Pardee, A. B. The restriction point of the cell cycle. *Cell Cycle* **1**, 102–109 (2002).

37. Ballabeni, A., Zamponi, R., Moore, J. K., Helin, K. & Kirschner, M. W. Geminin deploys multiple mechanisms to regulate Cdt1 before cell division thus ensuring the proper execution of DNA replication. *Proc. Natl. Acad. Sci. U. S. A.* **110**, 8–13 (2013).

38. McGarry, T. J. & Kirschner, M. W. Geminin, an inhibitor of DNA replication, is degraded during mitosis. *Cell* **93**, 1043–1053 (1998).

39. Luo, L. & Kessel, M. Geminin coordinates cell cycle and developmental control. *Cell Cycle* **3**, 709–712 (2004).

40. Dimaki, M. *et al.* Cell cycle-dependent subcellular translocation of the human DNA licensing inhibitor geminin. *J. Biol. Chem.* **288**, 23953–23963 (2013).

41. Massacci, G., Perfetto, L. & Sacco, F. The Cyclin-dependent kinase 1: more than a cell cycle regulator. *Br. J. Cancer* **129**, 1707–1716 (2023).

42. Ussar, S. & Voss, T. MEK1 and MEK2, different regulators of the G1/S transition. *J. Biol. Chem.* **279**, 43861–43869 (2004).

43. Hawkins, T. A., Cavodeassi, F., Erdélyi, F., Szabó, G. & Lele, Z. The small molecule Mek1/2 inhibitor U0126 disrupts the chordamesoderm to notochord transition in zebrafish. *BMC Dev. Biol.* **8**, 1–18 (2008).

44. Murad, H. *et al.* Induction of G1-phase cell cycle arrest and apoptosis pathway in MDA-MB-231 human breast cancer cells by sulfated polysaccharide extracted from Laurencia papillosa. *Cancer Cell Int.* **16**, 1–11 (2016).

45. Jin, M. *et al.* Cyclin A2/cyclin-dependent kinase 1-dependent phosphorylation of Top2a is required for S phase entry during retinal development in zebrafish. *J. Genet. Genomics* **48**, 63–74 (2021).

46. Xu, H. *et al.* Silencing of KIF14 interferes with cell cycle progression and cytokinesis by blocking the p27Kip1 ubiquitination pathway in hepatocellular carcinoma. *Exp. Mol. Med.* **46**, (2014).

47. Reilly, M. L. *et al.* Loss-of-function mutations in KIF14 cause severe microcephaly and kidney development defects in humans and zebrafish. *Hum. Mol. Genet.* **28**, 778–795 (2019).

48. Goshima, G., Nédélec, F. & Vale, R. D. Mechanisms for focusing mitotic spindle poles by minus end-directed motor proteins. *J. Cell Biol.* **171**, 229–240 (2005).

49. Ge, S. X., Jung, D., Jung, D. & Yao, R. ShinyGO: A graphical gene-set enrichment tool for animals and plants. *Bioinformatics* **36**, 2628–2629 (2020).

50. Deracinois, B., Flahaut, C., Duban-Deweer, S. & Karamanos, Y. Comparative and quantitative global proteomics approaches: An overview. *Proteomes* **1**, 180–218 (2013).

51. Van Engeland, M., Nieland, L. J. W., Ramaekers, F. C. S., Schutte, B. & Reutelingsperger, C. P. M. Annexin V-affinity assay: A review on an apoptosis detection system based on phosphatidylserine exposure. *Cytometry* **31**, 1–9 (1998).

52. Bossy-Wetzel, E. & Green, D. R. *Detection of Apoptosis by Annexin V Labeling*. *Methods in Enzymology* vol. 322 (ACADEMIC PRESS, 2000).

53. Logue, S. E., Elgendy, M. & Martin, S. J. Expression, purification and use of recombinant annexin V for the detection of apoptotic cells. *Nat. Protoc.* **4**, 1383–1395 (2009).

54. Pratama, E. *et al.* Critical role of ARID3B in the expression of pro-apoptotic p53-target genes and apoptosis. *Biochem. Biophys. Res. Commun.* **468**, 248–254 (2015).

55. Daddali, R., Ojaniemi, M., Hallman, M., Rämet, M. & Haapalainen, A. M. CPPED1-targeting microRNA-371a-5p expression in human placenta associates with spontaneous delivery. *PLoS One* **15**, 1–21 (2020).

56. Garcia, A. *et al.* Serine/threonine protein phosphatases PP1 and PP2A are key players in apoptosis. *Biochimie* **85**, 721–726 (2003).

57. Singh, P., Ravanan, P. & Talwar, P. Death associated protein kinase 1 (DAPK1): A regulator of apoptosis and autophagy. *Front. Mol. Neurosci.* **9**, 1–11 (2016).

58. Wang, S. *et al.* DAPK1 Signaling Pathways in Stroke: from Mechanisms to Therapies. *Mol. Neurobiol.* **54**, 4716–4722 (2017).

59. Zhang, T., Kim, B. M. & Lee, T. H. Death-associated protein kinase 1 as a therapeutic target for Alzheimer's disease. *Transl. Neurodegener.* **13**, 1–26 (2024).

60. Horikawa, I., Parker, E. S., Solomon, G. G. & Barrett, C. J. Upregulation of the gene encoding a cytoplasmic dynein intermediate chain in senescent human cells. *J. Cell. Biochem.* **82**, 415–421 (2001).

61. Hermeking, H. & Benzinger, A. 14-3-3 Proteins in Cell Cycle Regulation. *Semin. Cancer Biol.* **16**, 183–192 (2006).

62. Pennington, K., Chan, T., Torres, M. & Andersen, J. The dynamic and stress-adaptive signaling hub of 14-3-3: emerging mechanisms of regulation and context-dependent protein–protein interactions. *Oncogene* **37**, 5587–5604 (2018).

63. Mayer, M. L., Gygi, S. P., Aebersold, R. & Hieter, P. Identification of RFC(Ctf18p, Ctf8p, Dcc1p): An alternative RFC complex required for sister chromatid cohesion in S. cerevisiae. *Mol. Cell* **7**, 959–970 (2001).

64. Bermudez, V. P. *et al.* The alternative Ctf18-Dcc1-Ctf8-replication factor C complex required for sister chromatid cohesion loads proliferating cell nuclear antigen onto DNA. *Proc. Natl. Acad. Sci. U. S. A.* **100**, 10237–10242 (2003).

65. Thadani, R., Kamenz, J., Heeger, S., Muñoz, S. & Uhlmann, F. Cell-Cycle Regulation of Dynamic Chromosome Association of the Condensin Complex. *Cell Rep.* **23**, 2308–2317 (2018).

66. Chen, E. S., Sutani, T. & Yanagida, M. Cti1/C1D interacts with condensin SMC hinge and supports the DNA repair function of condensin. *Proc. Natl. Acad. Sci. U. S. A.* **101**, 8078–8083 (2004).

67. Griese, J. J., Witte, G. & Hopfner, K. P. Structure and DNA binding activity of the mouse condensin hinge domain highlight common and diverse features of SMC proteins. *Nucleic Acids Res.* **38**, 3454–3465 (2010).

68. Belew, M. D., Chen, J. & Cheng, Z. Emerging roles of cyclin-dependent kinase 7 in health and diseases. *Trends Mol. Med.* **31**, 138–151 (2024).

69. Olson, C. M. *et al.* Development of a Selective CDK7 Covalent Inhibitor Reveals Predominant Cell-Cycle Phenotype. *Cell Chem. Biol.* **26**, 792-803.e10 (2019).

70. Park, S. Y., Kim, K. Y., Jun, D. Y., Hwang, S. K. & Kim, Y. H. G1 cell cycle arrest and extrinsic apoptotic mechanisms underlying the anti-leukemic activity of cdk7 inhibitor bs-181. *Cancers (Basel).* **12**, 1–22 (2020).

71. Pellarin, I. *et al.* Cyclin-dependent protein kinases and cell cycle regulation in biology and disease. *Signal Transduct. Target. Ther.* **10**, 11 (2025).

72. Kimmel, C. B., Ballard, W. W., Kimmel, S. R., Ullmann, B. & Schilling, T. F. Stages of embryonic development of the zebrafish. *Dev. Dyn.* **203**, 253–310 (1995).

73. Shepard, J. L., Stern, H. M., Pfaff, K. L. & Amatruda, J. F. Analysis of the cell cycle in zebrafish embryos. *Methods Cell Biol.* **2004**, 109–125 (2004).

74. Faundes, V. *et al.* Impaired eIF5A function causes a Mendelian disorder that is partially rescued in model systems by spermidine. *Nat. Commun.* **12**, 1–13 (2021).

75. Suzuki, K., Bose, P., Leong-Quong, R. Y., Fujita, D. J. & Riabowol, K. REAP: A two minute cell fractionation method. *BMC Res. Notes* **3**, 294 (2010).

76. Rocco, L. Combined Exposure to TiO 2 Nanoparticles and Lincomycin. 1–13 (2022).

77. Perez-Riverol, Y. *et al.* The PRIDE database at 20 years: 2025 update. *Nucleic Acids Res.* **53**, D543–D553 (2025).

**Legends:**

**Figure 1: Cep57 localizes to the nucleus and spindle poles and is essential for early embryogenesis**

A: Whole-mount RNA *in situ* hybridization showing *cep57* expression during early development. Scale bars,100µm. B: RT-PCR analysis of *cep57* transcripts in different developmental stages. β-actin was used as the loading control. C: Sum projection confocal images of 256 cell stage WT embryos showing centrosomal staining by γ tubulin (red), Cep57 (green, red asterisks), and DNA (blue/DAPI). Scale bars, 50µm. D: Western blot showing localization of Cep57 in whole embryonic lysate, nuclear and cytoplasmic fractions. Lamin B1 was used to represent nuclear fractions, and Gapdh was used to represent cytoplasmic fractions. E: Western blot showing Cep57 levels in control and morpholino-injected embryos. Gapdh was used as the loading control. F: Quantification showing percent phenotype of cep57 splice morpholino injected, splice morpholino coinjected with cep57 mRNA, and cep57 mRNA only. Data are shown as mean ± SEM, n=3 for each experiment. G: Gross morphological analysis of *cep57* depleted embryos in comparison to control embryos at 10 somite and 24hpf stage showing somite architecture anomalies (red asterisk), midbrain-hindbrain boundary (double red asterisk), and body axis defects (red arrow). Scale bars, 100µm for 10 somite control and 50µm for 24hpf control embryos.

**Figure 2: *cep57* plays a key role in neural crest specification and mesodermal patterning**

Spatiotemporal gene expression analysis by *in situ* hybridization in control and *cep57* morphants at 6 somite and 24hpf stage. A, B, C: *Crestin, snail2,* and *sox10* expression in the 6 somite control and *cep57* (red asterisk) morphants. D, E, F: *Crestin, snail2,* and *sox10* expression in 24hpf control and *cep57* (double red asterisk) morphants. G: *Sox2* expression in 24hpf control and *cep57* (red asterisk) morphants. Scale bars, 100µm. H: *Tbxta* expression in 24hpf control and *cep57* (red arrow) morphants. Scale bar, 50µm.

**Figure 3: *cep57* depletion results in a microcephaly-like phenotype**

A: Whole mount skeletal preparations of 5dpf control and *cep57* morphant larvae showing cartilage and bone staining (red asterisk) using Alcian blue and Alizarin red S, respectively.

Scale bars, 100µm. B: Quantification of microcephaly-associated features – head area and interpupillary distance (IPD) in control and *cep57* morphants. C: Quantitative real-time PCR plots showing relative transcript levels of microcephaly markers *mcph1*, *wdr62*, *ankle2*, *map11*, *kif14*, and *aspm*. All data are shown as mean ± SEM. *p<0.05, **p<0.01, ***p<0.001. n=3 for each experiment.

**Figure 4: Cep57 is essential for cell cycle progression, and its depletion results in G1 arrest**
A: Whole mount acridine orange staining to visualize apoptotic cells (red asterisks) in control and *cep57* morphants. Scale bar, 100µm. B: PCR-based RAPD assay showing polymorphic bands (red arrow) in control and *cep57* morphants. C: Western blot showing Rad21 levels in control and morpholino-injected embryos. Gapdh was used as the loading control. D, E: Fluorescence-based flow cytometry analysis in control and cep57 morphants showing different phases of the cell cycle. F, G: Western blot showing Geminin, Cdk1, and Mek1 levels in control and morpholino-injected embryos. Gapdh was used as the loading control. H: Quantitative real-time PCR plots showing relative transcript levels of *p21*, *p27a*, and *p27b*. All data are shown as mean ± SEM. *p<0.05, **p<0.01, ***p<0.001. n=3 for each experiment.

**Figure 5: Cep57 maintains spindle pole integrity during embryonic mitoses and proteome profiling of *cep57* morphants**
A: Sum projection confocal images of 256 cell stage control and *cep57* morphant embryos showing microtubule and centrosomal staining at metaphase by α tubulin (red), γ tubulin (green, red asterisks) respectively, and DNA (blue/DAPI). B: Sum projection confocal images of 256 cell stage control and cep57 morphant embryos showing microtubule and centrosomal staining at interphase by α tubulin (red), γ tubulin (green, red asterisks) respectively, and DNA (blue/DAPI). Scale bars, 50µm. C: Quantification of *cep57* morphant embryos showing spindle pole focusing defects. D: GO analysis of differentially expressed proteins that are down-regulated in *cep57* morphants. E: GO analysis of differentially expressed proteins which are up-regulated in *cep57* morphants.

**Figure 6: Proposed model of *cep57* functions in cell cycle progression and embryonic development.**

A: Schematic representation showing *cep57* function in cell cycle progression. *cep57* depletion results in impaired cell cycle progression, G1 arrest, and increased apoptosis. B: *cep57* mediated cellular mechanisms underlying early neurodevelopment.

**Figure S1:**

A: Western blot showing cep57 levels in different developmental stages till 24hpf. Gapdh was used as the loading control. B: Quantification showing percent phenotype of control and *cep57* morphants injected with 1mM *cep57* translation blocker morpholino. Data are shown as mean ± SEM, n=3 for each experiment. C: Quantification showing percent phenotype of control and *cep57* morphants injected with 0.1mM and 0.5mM *cep57* translation blocker morpholinos. Data are shown as mean ± SEM, n=3 for each experiment. D: PCR-based validation of intron retention in *cep57* morphants injected with splice morpholino and rescue of splicing event when coinjected with in vitro transcribed cep57mRNA. mRNA alone injected embryos showed correct splicing. No template control (NTC) was used as a negative control. E: Gross morphological analysis of *cep57* morphants P0, P1, P2, and P3 at different stages of larval development.

**Figure S2:**

A: *Pax2a* expression in the 24hpf control and *cep57* morphants. B: *Egr2b* expression in the 24hpf control and *cep57* morphants. C: *Myod1* expression in the 24hpf control and *cep57* morphants.

**Figure S3:**

A, B: Western blot showing Separase and Cyclin E levels in different developmental stages till 24hpf. Gapdh was used as the loading control. C: Sum projection confocal images of 256 cell stage control and cep57 morphant embryos showing mitotic cells by PH3 (green) and DNA (blue/DAPI). Scale bars, 50µm. C, D: GO analysis of all the upregulated and downregulated proteins in cep57 morphants, respectively.

**Figure S4:**

List of all the primers used in this study.

**Figure S5:**

List of all the antibodies used in this study.

# Figure 1

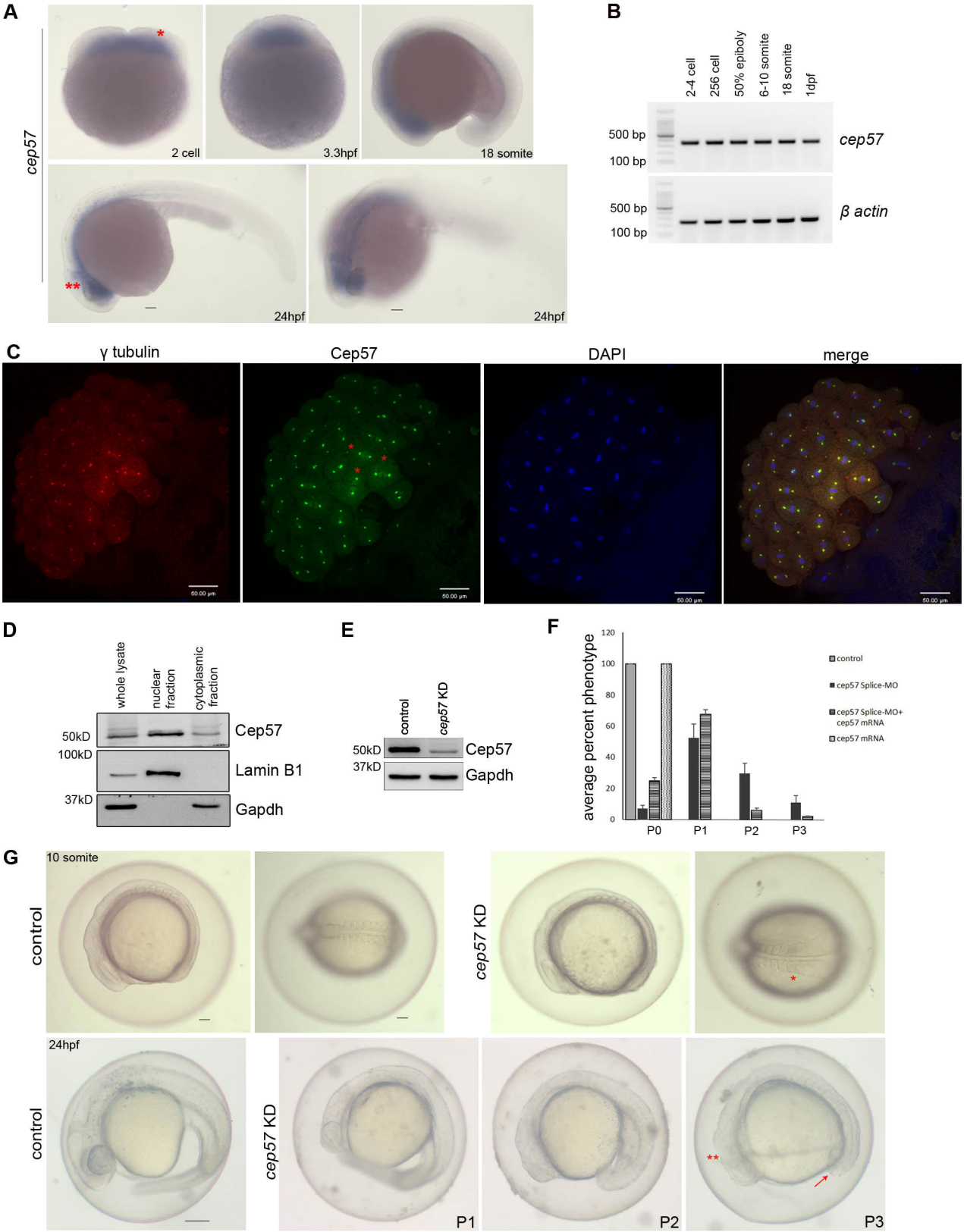
A
cep57
2 cell
3.3hpf
18 somite
24hpf
24hpf
B
2-4 cell
256 cell
50% epiboly
6-10 somite
18 somite
1dpf
500 bp
100 bp
cep57
500 bp
100 bp
β actin
C
γ tubulin
Cep57
DAPI
merge
D
whole lysate
nuclear fraction
cytoplasmic fraction
50kD
100kD
37kD
Cep57
Lamin B1
Gapdh
E
control
cep57 KD
50kD
37kD
Cep57
Gapdh
F
average percent phenotype
control
cep57 Splice-MO
cep57 Splice-MO+ cep57 mRNA
cep57 mRNA
P0
P1
P2
P3
G
10 somite
control
cep57 KD
24hpf
control
cep57 KD
P1
P2
P3

# Figure 2

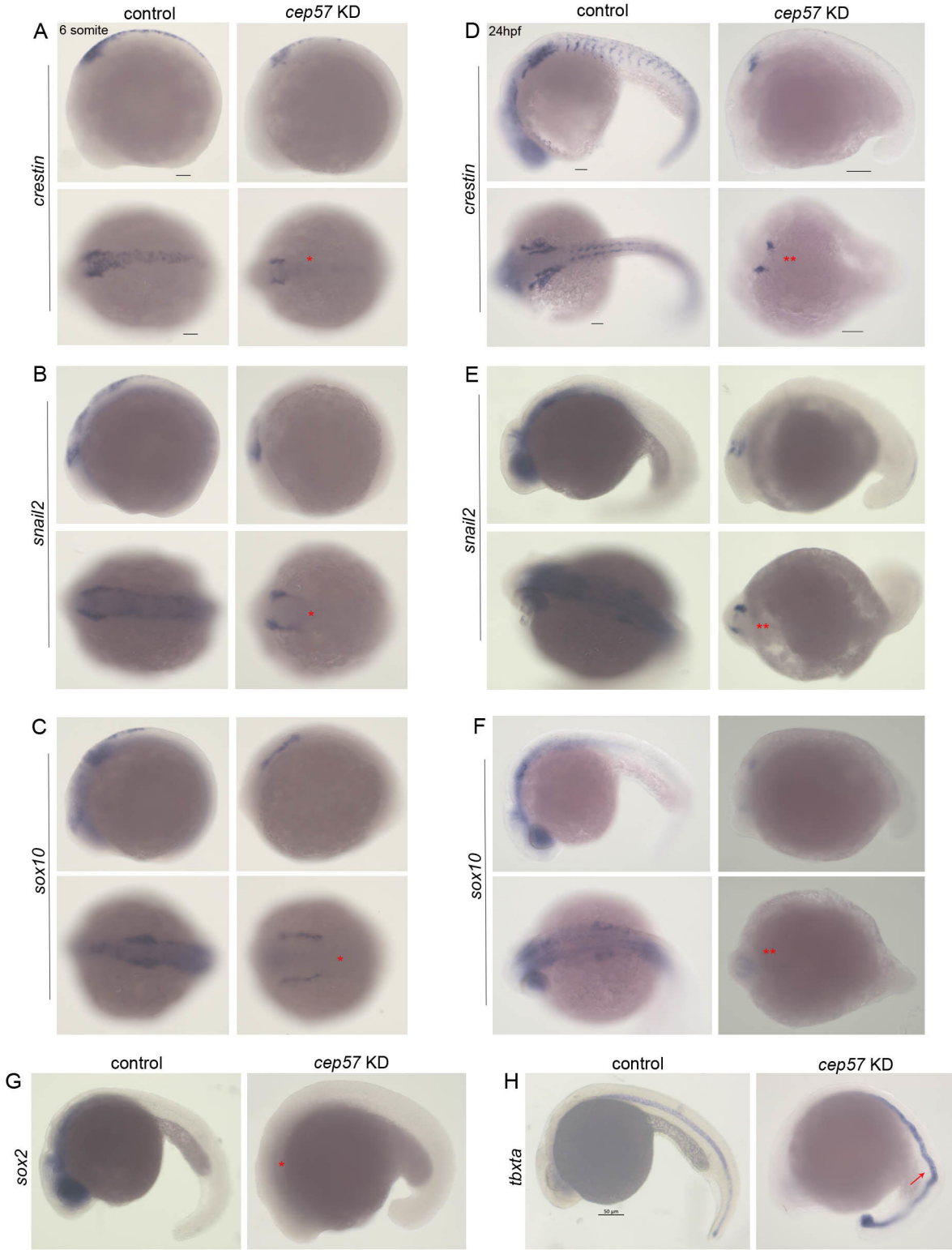
A
6 somite
control
cep57 KD
crestin
B
snail2
C
sox10
D
24hpf
control
cep57 KD
crestin
E
snail2
F
sox10
G
control
cep57 KD
sox2
H
control
cep57 KD
tbxta
50 µm

# Figure 3

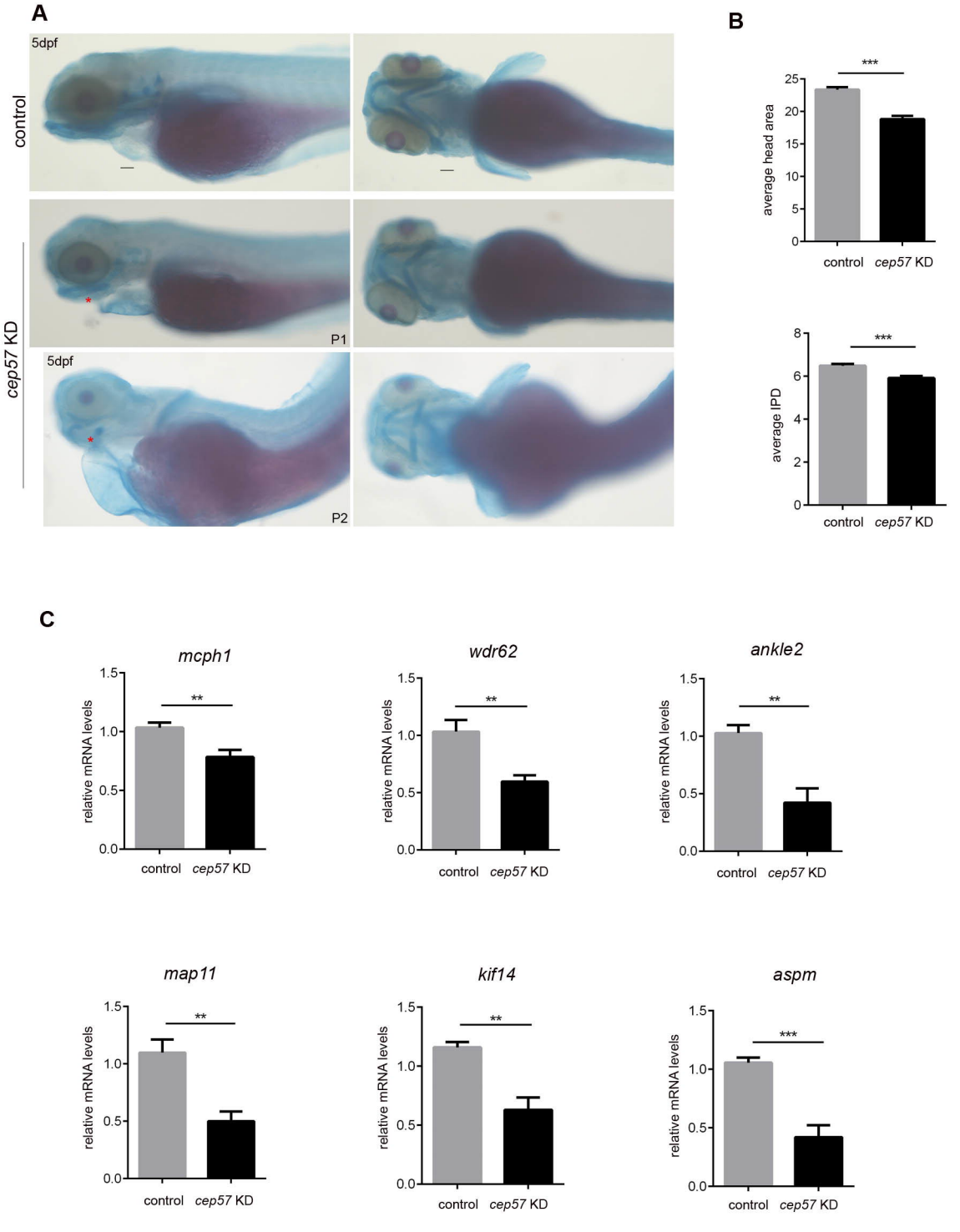
A
5dpf
control
cep57 KD
P1
5dpf
P2
B
average head area
***
control
cep57 KD
average IPD
***
control
cep57 KD
C
mcph1
wdr62
ankle2
map11
kif14
aspm
relative mRNA levels
**
***
control
cep57 KD

# Figure 4

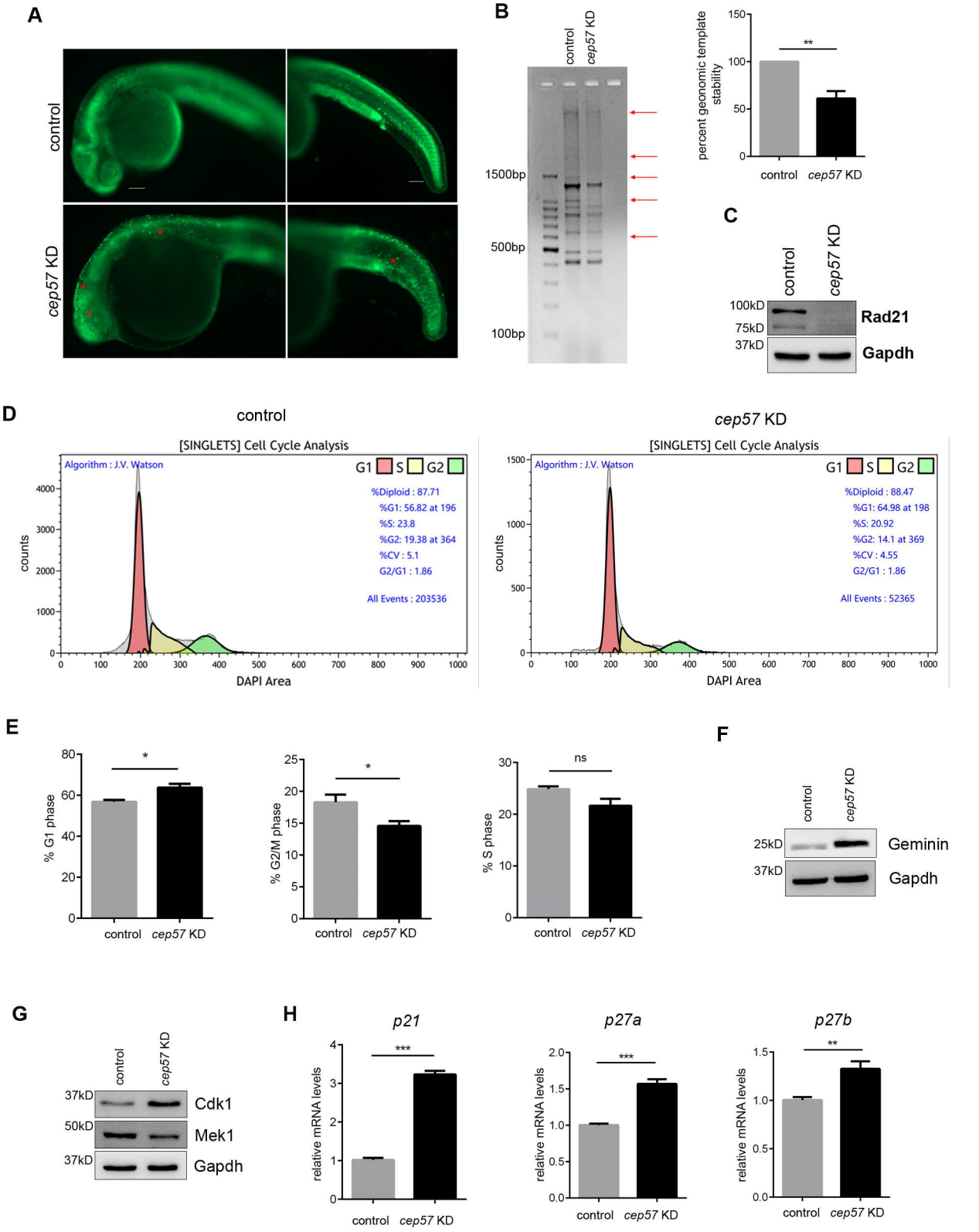
A
control
cep57 KD
B
control
cep57 KD
1500bp
500bp
100bp
percent genomic template stability
150
100
50
0
**
control
cep57 KD
C
control
cep57 KD
100kD
75kD
37kD
Rad21
Gapdh
D
control
[SINGLETS] Cell Cycle Analysis
Algorithm : J.V. Watson
G1 S G2
%Diploid : 87.71
%G1: 56.82 at 196
%S: 23.8
%G2: 19.38 at 364
%CV : 5.1
G2/G1 : 1.86
All Events : 203536
counts
DAPI Area
cep57 KD
[SINGLETS] Cell Cycle Analysis
Algorithm : J.V. Watson
G1 S G2
%Diploid : 88.47
%G1: 64.98 at 198
%S: 20.92
%G2: 14.1 at 369
%CV : 4.55
G2/G1 : 1.86
All Events : 52365
counts
DAPI Area
E
% G1 phase
*
control
cep57 KD
% G2/M phase
*
control
cep57 KD
% S phase
ns
control
cep57 KD
F
control
cep57 KD
25kD
37kD
Geminin
Gapdh
G
control
cep57 KD
37kD
50kD
37kD
Cdk1
Mek1
Gapdh
H
p21
relative mRNA levels
***
control
cep57 KD
p27a
relative mRNA levels
***
control
cep57 KD
p27b
relative mRNA levels
**
control
cep57 KD

# Figure 5

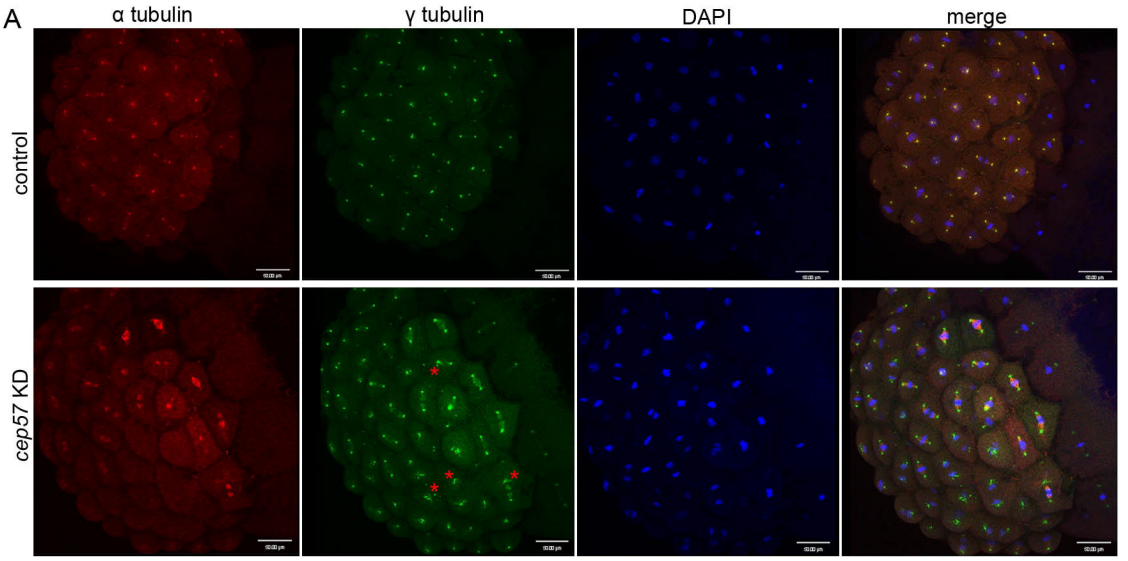
A
α tubulin
γ tubulin
DAPI
merge
control
cep57 KD

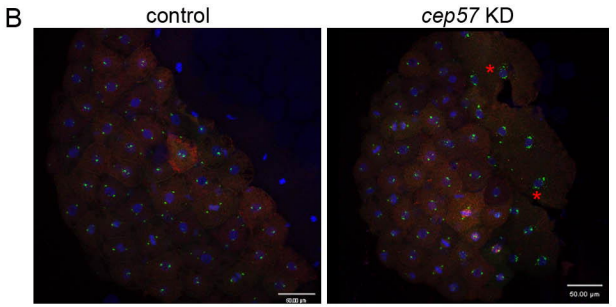
B
control
cep57 KD

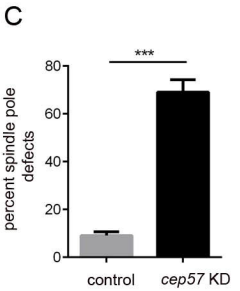
C
***
percent spindle pole defects
80
60
40
20
0
control
cep57 KD

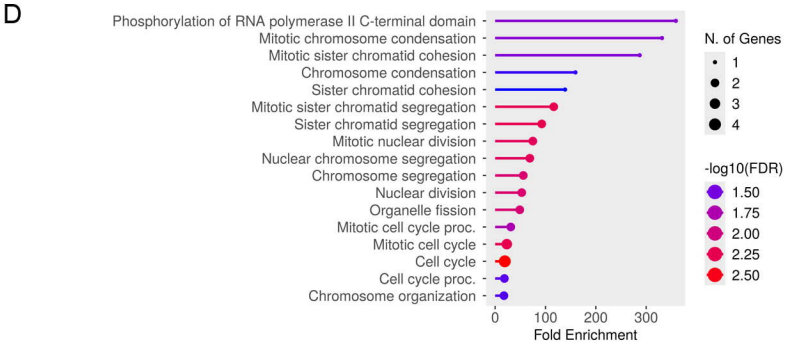
D
Phosphorylation of RNA polymerase II C-terminal domain
Mitotic chromosome condensation
Mitotic sister chromatid cohesion
Chromosome condensation
Sister chromatid cohesion
Mitotic sister chromatid segregation
Sister chromatid segregation
Mitotic nuclear division
Nuclear chromosome segregation
Chromosome segregation
Nuclear division
Organelle fission
Mitotic cell cycle proc.
Mitotic cell cycle
Cell cycle
Cell cycle proc.
Chromosome organization
0
100
200
300
Fold Enrichment
N. of Genes
1
2
3
4
-log10(FDR)
1.50
1.75
2.00
2.25
2.50

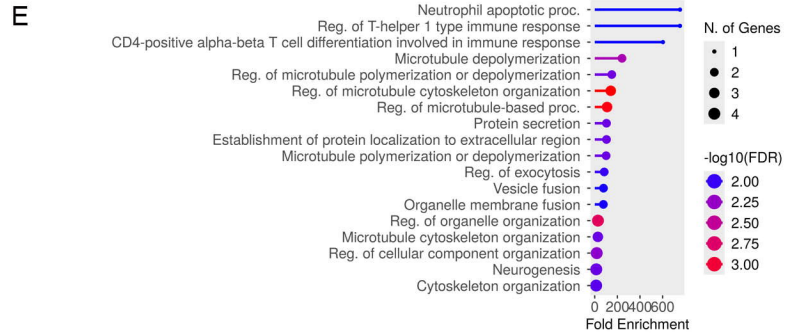
E
Neutrophil apoptotic proc.
Reg. of T-helper 1 type immune response
CD4-positive alpha-beta T cell differentiation involved in immune response
Microtubule depolymerization
Reg. of microtubule polymerization or depolymerization
Reg. of microtubule cytoskeleton organization
Reg. of microtubule-based proc.
Protein secretion
Establishment of protein localization to extracellular region
Microtubule polymerization or depolymerization
Reg. of exocytosis
Vesicle fusion
Organelle membrane fusion
Reg. of organelle organization
Microtubule cytoskeleton organization
Reg. of cellular component organization
Neurogenesis
Cytoskeleton organization
0
200
400
600
Fold Enrichment
N. of Genes
1
2
3
4
-log10(FDR)
2.00
2.25
2.50
2.75
3.00

# Figure 6

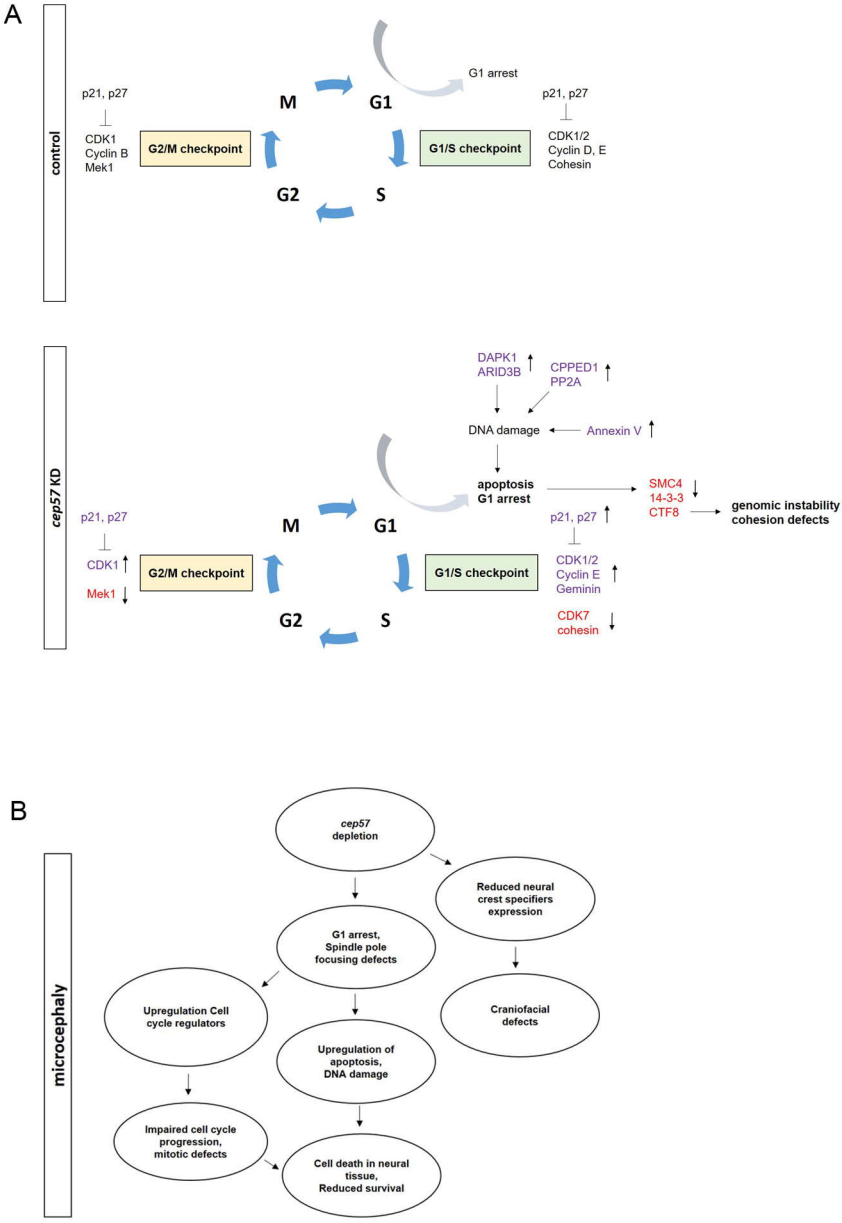
A
control
p21, p27
CDK1
Cyclin B
Mek1
G2/M checkpoint
M
G1
G1 arrest
p21, p27
CDK1/2
Cyclin D, E
Cohesin
G1/S checkpoint
G2
S
cep57 KD
DAPK1
ARID3B
CPPED1
PP2A
DNA damage
Annexin V
apoptosis
G1 arrest
SMC4
14-3-3
CTF8
genomic instability
cohesion defects
p21, p27
CDK1
Mek1
G2/M checkpoint
M
G1
p21, p27
CDK1/2
Cyclin E
Geminin
G1/S checkpoint
CDK7
cohesin
G2
S
B
microcephaly
cep57
depletion
Reduced neural
crest specifiers
expression
G1 arrest,
Spindle pole
focusing defects
Upregulation Cell
cycle regulators
Craniofacial
defects
Upregulation of
apoptosis,
DNA damage
Impaired cell cycle
progression,
mitotic defects
Cell death in neural
tissue,
Reduced survival